Turk J Phys
28 (2004) , 121 – 132.

Structural and Magnetic Properties of $Co_{0.6}ZnN_{0.4}Mn_xFe_{2-x}O_4$

O. M. HEMEDA
Physics Department, Faculty of Science, Tanta University, EGYPT

Received 07.08.2003

Abstract

A series of Co-Zn ferrite samples substituted by Mn were prepared by the usual double sintering ceramic technique. The x-ray diffraction patterns of the samples confirmed the formation of single-phase spinel structure, and x-ray analysis supply data that suggests the cation distribution of the material. The tetrahedral and octahedral radius permits one to calculate the theoretical lattice parameter and the bond lengths Fe-O at A and B sites. The particle size of the given samples was measured from the Scherer equation and a correlation was found between particle size, and structural and magnetic properties. The XRF confirmed the presence of stoichiometric solid-state reaction in the material. The saturation magnetization M_s decreases continuously with increase of Mn content. For $Co_{0.6}\,Zn_{0.4}\,Mn_x\,Fe_{2-x}\,O_4$, the Neel model for the two sub-lattice can be used up to $x = 0.8$ to explain the compositional variation of magnetic moment due to the reduction of the $A - B$ interaction. Above $x = 0.8$, the reduction of the B-B interaction is responsible for an increase in the magnetic moment due to the canting effect.

Key Words: Co-Zn-Mn ferrite, Cation distribution, Magnetic properties.

1. Introduction

Structural and magnetic properties of spinel ferrites depend upon the method of preparation, nature of dopant and dopant concentration. Mn-Zn ferrite is extensively used in high frequency applications up to 10 MHz [1–3]. Several researchers have studied the magnetic properties of Mn-Zn ferrite as a function of temperature [4] and grain size [5]. The magnetic moment of Mn ferrite ($MnFe_2O_4$) agrees with the Neel coupling scheme [6], and has a much lower resistivity than $CoFe_2O_4$ and $NiFe_2O_4$ [7]. Using neutron diffraction, Yamzin et al. [8] measured the distribution of manganese among tetrahedral and octahedral sites in $Mn_{1-x}\,Fe_{2-x}O_4$ and found that 30 percent of the octahedral sits are occupied by Mn^{3+} with the distribution $Mn^{2+}_{0.9}\,Fe^{3+}_{0.1}\left[Mn^{3+}_{0.6}\,Fe^{3+}_{1.3}\,Fe^{2+}_{0.1}\right]\,O_4$.

The manganese ferrite is nearly normal spinel, where about 80% of Mn^{2+} ion occupy the tetrahedral A sites. However, there are Mn^{3+} ions at the octahedral B sites, and are connected by the presence of Fe^{2+} ions also present at these sites [9].

This present research was carried out with the following goals.

Fabricate various spinel ferrites by ceramic method.

Investigate the correlation between the structural parameters and substituted Mn ions.

Study the occupancy of various ions at tetrahedral and octahedral sites.

Investigate the magnetic behavior of the samples by measuring the saturation magnetization, and magnetic moment.

Determine the order of spin canting via calculations of the Yafet-Kittel angles.

2. Experimental Procedure

The samples of stoichiometric composition $Co_{0.6}Zn_{0.4}Mn_xFe_{2-x}O_4$,$0 \leq \quad x \quad \leq 1$, were prepared via the usual double sintering ceramic technique. Pure oxides were mixed and grounded in to a very fine powder. The mixture was heat treated at 900 $^\circ$ C for 10 h and then cooled to room temperature. The powder was again grounded and re-powdered over 10 hours, gradually. The mixture was sintered for the final time at 1300 °C for four hours and then slowly cooled to room temperature. The single phase formation of the ferrite sample was confirmed by x-ray diffraction patterns obtained by using a Philips PW 1710 diffractometer employing CuK$_a$ radiation (λ = 1.5405 Å). The x-ray density was determined using the formula $D_x = (8M/N_Aa^3)$, where M is the Molecular weight, N_A is Avogadro's number and a is the lattice constant. The elemental composition of the samples was measured using a HNU Instruments TEFA-PC Energy Dispersive x-ray fluorescence (ED-XRF) analyzer, consisting of an x-ray spectrometer and sample chamber. The x-ray tube used in the present study worked with a molybdenum anode at 20 kV. The magnetization measurements were carried out at room temperature using an automated Oxford vibrating-sample magnetometer (VSM).

3. Results and Discussion

3.1. Cation distribution studies

The spinel structure has been extensively dealt with by Gorter [10]. The unit cell of the ideal spinel structure is given in Figures. 1a and 1b. The anions form a cubic closed pack in which cations partly occupy the tetrahedral and octahedral interstices. These are respectively called A and B sites, with space group $O_h^7 - F_3$ dm [11]. The unit cell contains 32 anions formatting 64 tetrahedral interstitial sites and 32 octahedral sites, out of which 8 tetrahedral and 16 octahedral sites are occupied by cations.

XRD patterns of $Co_{0.6}Zn_{0.4}Mn_xFe_{2-x}O_4$ for the samples with x = 0.0, 0.1, 0.2, 0.3, 0.4, 0.5, 0.6, 0.7, 0.8, 0.9 and 1.0, are shown in Figure 1. The patterns were indexed and cubic lattice was observed. The results indicate that the material has a well-defined crystalline single phase belonging to the fcc system. The diffraction pattern gave a verification of the presence of spinel crystal structure for each composition of $Co_{0.6}Zn_{0.4}Mn_xFe_{2-x}O_4$. The structural parameters for different concentration are listed in Table 1.

Table 1. The x-ray parameters for the given samples.

Mn content (x)	MW (gm)	Cation distribution	U	δ	P (Å)	q (Å)	$\overline{D}$ (nm)
0	237.20	$(Zn^{2+}_{0.4}Fe^{3+}_{0.6})[Co^{2+}_{0.6}Fe^{3+}_{1.4}]$	0.387	0.012	1.999	2.01	24.5
0.1	237.11	$(Zn_{0.4}Fe^{3+}_{0.542}Mn^{2+}_{0.058})[Co^{2+}_{0.6}Mn^{3+}_{0.042}Fe^{3+}_{1.358}]$	0.388	0.013	2.003	1.993	24.52
0.2	237.02	$(Zn_{0.4}Mn_{0.116}Fe_{0.484})[Co_{0.6}Mn_{0.084}Fe_{1.316}]$	0.389	0.014	2.018	1.985	24.7
0.3	236.93	$(Zn_{0.4}Mn_{0.174}Fe_{0.426})[Co_{0.6}Mn_{0.126}Fe_{1.274}]$	0.3895	0.0145	2.02	1.976	24.75
0.4	236.84	$(Zn_{0.4}Mn_{0.232}Fe_{0.368})[Co_{0.6}Mn_{0.168}Fe_{1.232}]$	0.3898	0.0148	2.034	1.956	24.75
0.5	236.74	$(Zn_{0.4}Mn_{0.29}Fe_{0.31})[Co_{0.6}Mn_{0.21}Fe_{1.19}]$	0.3899	0.0149	2.033	1.98	24.8
0.6	236.65	$(Zn_{0.4}Mn_{0.35}Fe_{0.25})[Co_{0.6}Mn_{0.25}Fe_{1.15}]$	0.3916	0.0166	2.075	1.985	24.87
0.7	236.56	$(Zn_{0.4}Fe_{0.19}Mn_{0.41})[Co_{0.6}Mn_{0.29}Fe_{1.11})$	0.3917	0.0167	2.078	1.986	24.9
0.8	236.47	$(Zn_{0.4}Mn_{0.47}Fe_{0.13})[Co_{0.6}Mn_{0.33}Fe_{1.07}]$	0.3925	0.0175	2.095	1.985	24.95
0.9	236.38	$(Zn_{0.4}Mn_{0.52}Fe_{0.08})[Co_{0.6}M_{0.38}Fe_{1.02}]$	0.3927	0.0177	2.101	1.988	25.7
1	236.29	$(Zn_{0.4}Mn_{0.58}Fe_{0.02})[Co_{0.6}Mn_{0.42}Fe_{0.98}]$	0.393	0.018	2.109	1.987	30.54

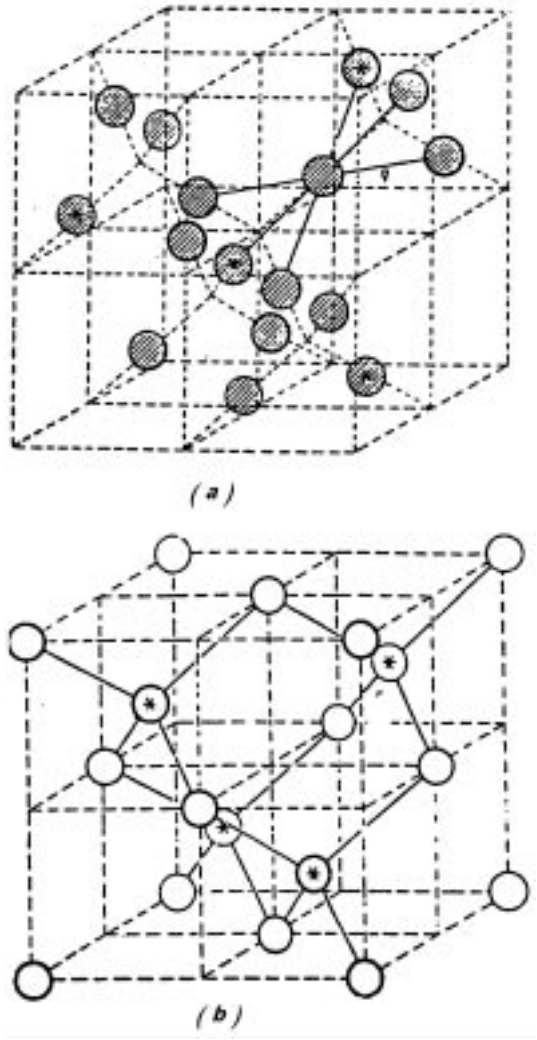

Figure 1. The geometry of the spinel ferrite unit cell.

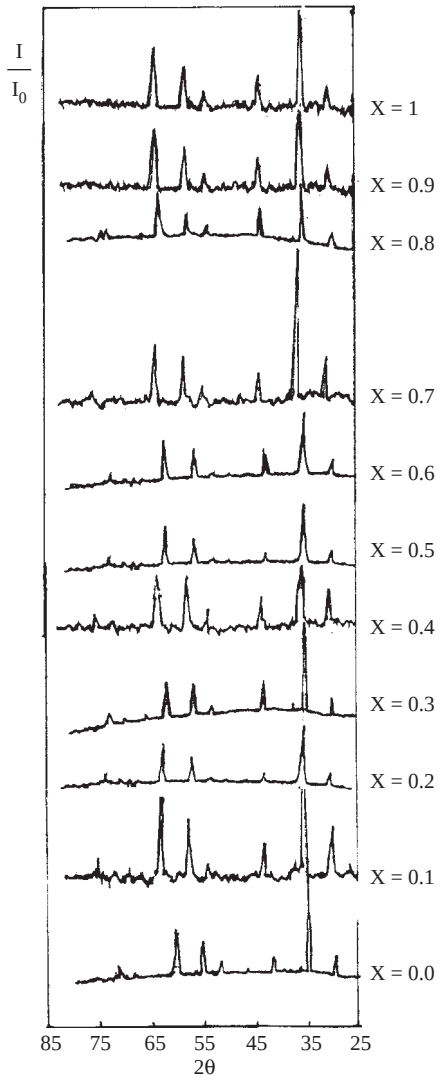

Figure 2. The x-ray diffraction patterns for the studied samples.

The theoretical (a_{th}) and experimental(a_{ex}) values of the lattice parameter, the radius of tetrahedral site r_A and the octahedral sites r_B have been calculated and are plotted as a function of Mn content x and are shown in Figures. 3 and 4. The a_{th} has values near a_{ex} at high concentrations of Mn, but are different at values$x \leq 0.5$. This means that there is a deviation from the ideal formula of cation distribution due to the presence of some Mn^{4+} with radius = 0.052 nm. Figure 4 Shows that r_A increases with x, butr_B remains constant. The substitution of Mn^{2+} with radius 0.068 nm for Fe^{3+} with radius 0.064 at tetrahedral sites leads to the increase of r_A. The presence of Mn^{3+} with radius 0.068 nm Fe^{3+} at octahedral sites does not change the r_B values. The variation of the bond length p, q with Mn content (given in Table 1); where p is the shortest distance between A site cation and the oxygen ion, and q is the shortest distance between B site cations and oxygen ions. The bond length was calculated using the relations [12]

$$q = a\sqrt{3}(\delta + \frac{1}{8}) \quad p = a\left(3\delta^2 - \frac{\delta}{2} + \frac{1}{16}\right)^{1/2}, \tag{1}$$

where $\delta = (\ u - 0.375)$ and u is the oxygen positional parameter. The value of u is given by the following relations (12):

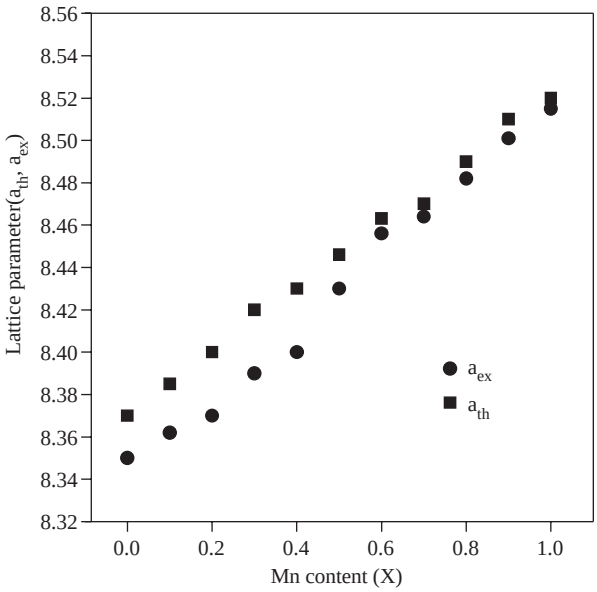

Figure 3. The experimental and theoretical lattice parameters as a function of Mn content.

$$r_A = (u - \frac{1}{4})\sqrt{3}a - R_o$$
$$r_B = (\frac{5}{8} - 4)a - R_o, \tag{2}$$

where R_o is the radius of the oxygen ions. The values of p and q increase with Mn content, a characteristic which can be attributed to the increase in lattice parameter. Levine [13] has suggested that there exists an inverse relationship between the covalent character of the spinel structure and bond lengths. Since p and q increases with Mn content, it can be concluded that the covalent character of the spinel structure decreases as well. Similar results have been reported in the case of Li-Cd and Cu-Zn ferrites [14, 15].

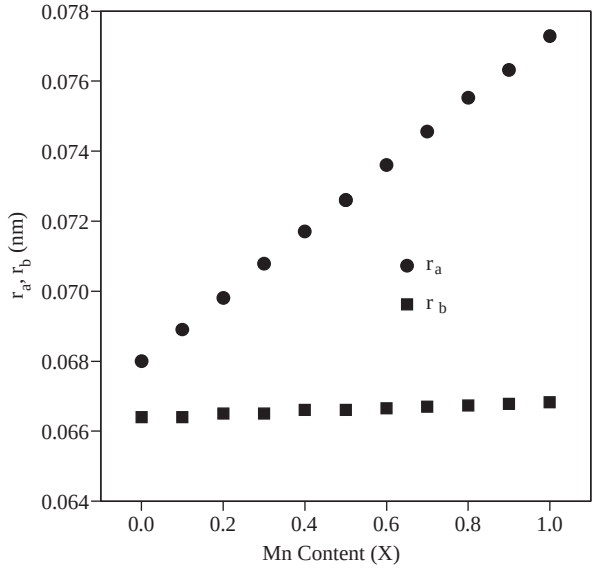

Figure 4. The radius of tetrahedral and octahedral sites as a function of Mn content.

The theoretical lattice parameter can be calculated using the values of r_A, r_B and R_o. In order to calculate r_A and R_B it is necessary to know the cation distribution, which can be represented by the formula

$$\left(Zn_{0.4}Fe_{0.6}Mn_t^{2+}\right)\ \left[Co_{0.6}^{2+}Mn_{x-t}^{3+}Fe_{1.4-x+t}^{3+}\right],$$

where t is the fraction of divalent Mn^{2+} ions at tetrahedral sites and was found to be $t = 0.58$. The ionic radius can be calculated from the following relations:

$$\begin{aligned} r_A &= 0.4\, r_{Zn^{2+}} + (06-t)r_{Fe^{3+}} + t r_{Mn^{2+}} \\ r_B &= \tfrac{1}{2}[0.6 r_{Co^{2+}} + (x-t)r_{Mn^{3+}} + (1.4-x+t)r_{Fe^{3+}}]. \end{aligned} \tag{3}$$

As known, Co^{2+} and Mn ions prefer position at octahedral sites while Zn ions prefer tetrahedral sites. The different cation distributions could result in the agreement between the theoretical and experimental lattice parameters. These cation distributions are given in Table 1, column 3.

According to the distribution formula, 58% of Mn content as divalent ions occupies tetrahedral sites and the remainder of the Mn content occupies octahedral sites as trivalent ions.

3.2. Oxygen positional parameter u and inversion parameter δ

Suppose the cations and anions are spheres. The A site is smaller in size than the B sites. A site is unable to accommodate available cations without local distortion of the sites. Thus each A site expands by an equal displacement of the four surrounding oxygen ions, towards and along the body diagonal of the cube, to form a tetrahedral with an $A-$ion having cubic symmetry. However, six oxygen ions surrounding a B site are shifted in such a way that this oxygen octahedral shifts by the same amount, as the first expands.A quantitative measure of this displacement is the oxygen positional parameter u, given by a distance between an oxygen ion and a face of a cube. The ideal FCC parameter is $u = \frac{3}{8} = 0.375$, where the packing of ions, within the lattice, is taken as perfect. However, slight deviation from the perfect value may occur due to relatively larger oxygen ion which causes a small distortion of the lattice structure to make space for the cations at the available interstitial sites in the unit cell.

The oxygen atom in the spinel structure is not generally located at the exact FCC sub lattice. Their detailed positions are deformed as given by the u parameter, which reflect adjustment of the structure to accommodate differences in the radius ratio of the cation in A and B sites. The u value for spinel ferrite ranges between 0.375 and 0.385. It has been reported that, for divalent ions at tetrahedral sites, the u value is 0.387 but the ideal u value for the trivalent ions at A sites is 0.381. When parameter u is less than the ideal case ($u = 0.375$) it is assumed that the origin was taken at one of octahedral sites, not at tetrahedral sites.

The results of the calculation of inversion parameter δ, and oxygen positional parameter for Co-Zn-Mn ferrite are presented in Table 1, where $\delta = u-$ 0.375 is the deviation from the ideal u-parameter. The spinel ferrite has u parameter slightly above 0.375. The value of u parameter for the studied samples increases from 0.387 to 0.393 in going from $x = 0$ to 1.0, while the value of δ increases from 0.012 to 0.018. The increase in u parameter may be due to the shift of the origin at the tetrahedral sites with the decreasing number of Fe ion at the octahedral sites. (That is, the distortion of the lattice, and the deviation from FCC ideal case, increases with Mn content). The cation distribution for each sample shows the presence of Mn ions at either A and B sites. Accordingly the Mn ferrite belongs to the family of inverse and normal ferrites. Negative deviation from Vegard's low (which means a linear relationship between the increase of the lattice parameter and the addition content) occur when the same ion is present at different crystallographic positions with different chemical bonds. The rate of the increase for lattice constant with Mn content is greater than that of normal ferrite (0.015) and smaller than 0.04 for the inverse ferrite.

3.3. Grain Size

Figure 5 shows the average grain size D as a function of Mn content; and that the average grain size $\overline{D}$ increases with Mn content. The grain size is inversely proportional to the line width for diffraction peaks. The average grain size were calculated using the Scherer equation [16] $\overline{D} = k\lambda/h_{1/2}Cos\,\theta$, where $k = 51.57$ is the Scherer constant, $\lambda = 1.5405$ Å is the wavelength of the CuK_α radiation, $h_{1_{/2}}$ is the peak width at half maximum and θ corresponds to the peak position. It has been found that the ferrite usually requires a volume distribution upper limit < 50 nm and a concentration of at least 13% Fe, to be spinel. The volume distribution showed that the particle size ranged from 21.3–28.9 nm with an average of 24.89 nm for $x = 0.6$; from 22–26 nm with an average of 24.1 nm for $x = 0.7$; 18–32 nm with an average of 24.86 nm for $x = 0.8$; 20.5–38 nm with an average of 25.7 nm for $x = 0.9$; and 24.6–37.2 nm with an average of 30.54 nm for $x = 1.0$. All the grain size was within the spinel limits. The upper limit of grain size is very important for successful spinning.

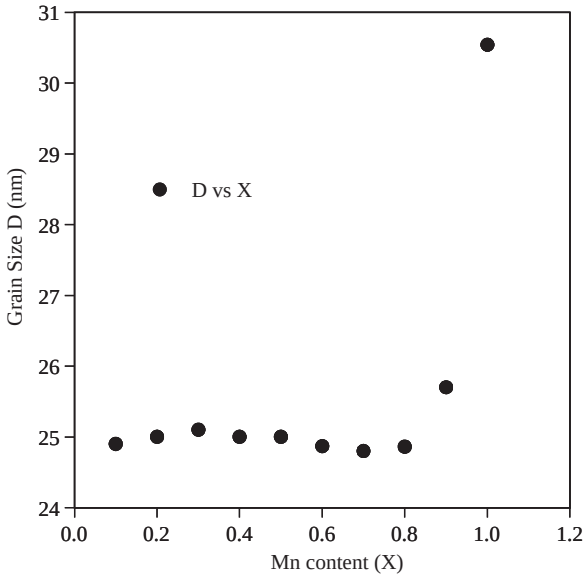

Figure 5. The grain size as a function of Mn content.

Figure 6 shows the x-ray density D_x and bulk density as a function of Mn content, the former increasing as the latter increases. Note that the atomic weight of Mn, at 54.9, is lower than that of Fe^{3+} (at 55.85). The porosity of the samples increases with $x$and varies from 0.07 to 0.18. The porosity p was calculated using the relation

The bulk density decreases from 4.8 for $x = 0.0$ to 4.2 g/cm^3 for x = 1 and the grain size increase from 24.8 to 30.54 nm. As the grain size increases the density decrease, the porosity increases. The inter-granular pores as developed during sintering must also be capable of moving with the grain boundaries as growth occurs.

3.4. X-ray fluorescence

The elemental composition of the samples was measured by x-ray fluorescence (XRF), and is shown in Table 2.

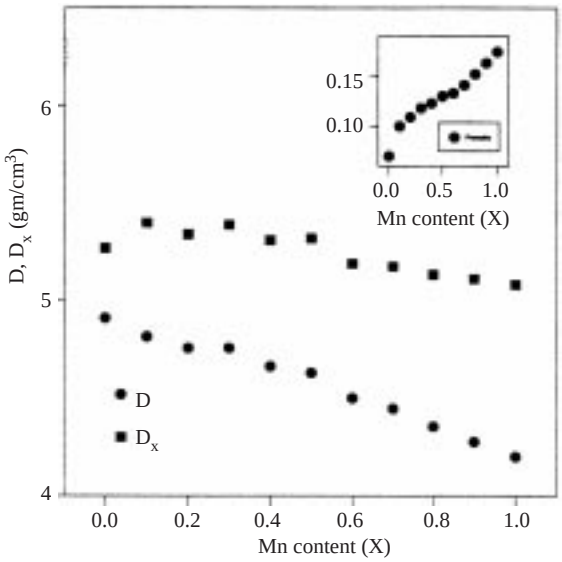

Figure 6. The x-ray density, bulk density and the porosity as a function of Mn content.

$$P = \left(1 - \frac{D}{D_x}\right). \tag{4}$$

Table 2. The samples compositions as given from XRF.

Mn content	Composition
$x = 0.6$	$Co_{0.6}Zn_{0.4}Fe_{1.39}Mn_{0.61}O_4$
$x = 0.8$	$Co_{0.6}Zn_{0.4}Fe_{1.215}Mn_{0.785}O_4$
$x = 0.9$	$Co_{0.6}Zn_{0.4}Fe_{1.076}Mn_{0.924}O_4$
$x = 1.0$	$Co_{0.6}Zn_{0.4}Fe_{0.95}Mn_{1.05}O_4$

The XRF spectrum for samples $x = 0.6$, 0.7, 0.8 and 0.9 are shown in Figure 7. The composition weight (in %) and net intensity associated with the Fe-K_α line for various elements are given in Table 3.

Table 3. The XRF analysis data.

	$x = 0.6$		$x = 0.7$		$x = 0.9$		$x = 1.0$	
Element Element	Weight, %	Net intensity	Weight, %	Net intensity	Weight, %	Net intensity	Weight, %	Net intensity
Mn	6.820	351.76	17.386	731.74	19.599	863.93	21.896	977.59
Fe	57.444	2278.47	48.146	1703.52	45.646	1718.09	43.469	1683.28
Co	18.854	696.23	17.656	510.64	17.732	531.31	17.493	525.36
Zn	16.883	241.44	16.812	214.99	17.023	231.46	17.143	239.88

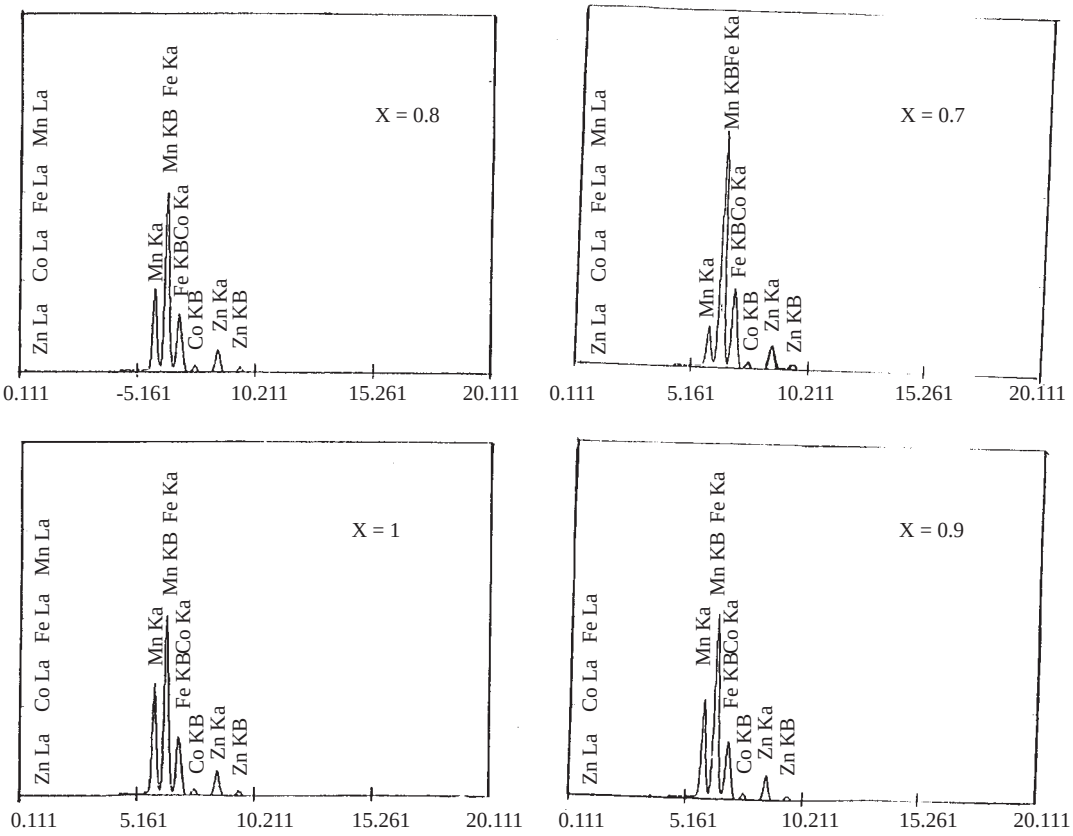

Figure 7. XRF of the samples $x = 0.7$, 0.8, 0.9, and 1.

Note that, with increasing Mn content, the intensity of the FeK_α line decreases, the MnK_α line increases, whereas the Co and Zn lines are nearly the same for all samples. The MnK_β line overlaps with the FeK_α line. The XRF spectra show the presence of the Fe, Mn, Co, and Zn and there are no other traces of other oxides, indicating the high purity of the oxides used.

3.5. Magnetic Properties

The magnetic properties of $Co_{0.6}\,Zn_{0.4}\,Mn_x\,Fe_{2-x}\,O_4$ have been investigated by magnetization hysteresis curve measurements at room temperature. The initial magnetization curves for all samples are shown in Figure 8. The magnetization curves shift to lower values as Mn content increases since the magnetic moment of Mn^{2+} is lesser than that of Fe^{3+}, resulting in the decrease of the A-B interaction. The saturation magnetizations $\sigma_s$in emu /g for all samples were taken from the M-H loop .The saturation magnetization M_s in (emu/cc) was calculated by using the formula $M_s = (1 - P)\sigma_s\ d_s$, where P and d_s are the porosity and density of the samples, respectively. The saturation magnetization σ_s (emu /g) was plotted against Mn content as shown in Figure 9. The variation of the saturation magnetization $\sigma_s$can be explained on the basis of cation distribution and exchange interaction. The Mn ions substitute Fe^{3+} as Mn^{2+} at tetrahedral and as Mn^{3+} at octahedral sites, which decrease the inverse character of the studied ferrite, as shown in x-ray analysis. σ_s decreases as the inversion parameter δ increases from 0.012 to 0.018, the $A - B$ negative interaction decreases and consequently saturation magnetization decreases. Above $x = 0.8$, $\sigma_s$increases and A-B interaction increases.

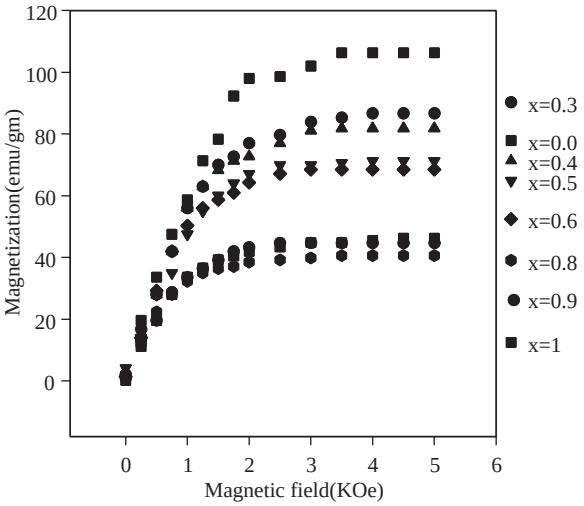

Figure 8. The initial magnetization curves for the studied samples.

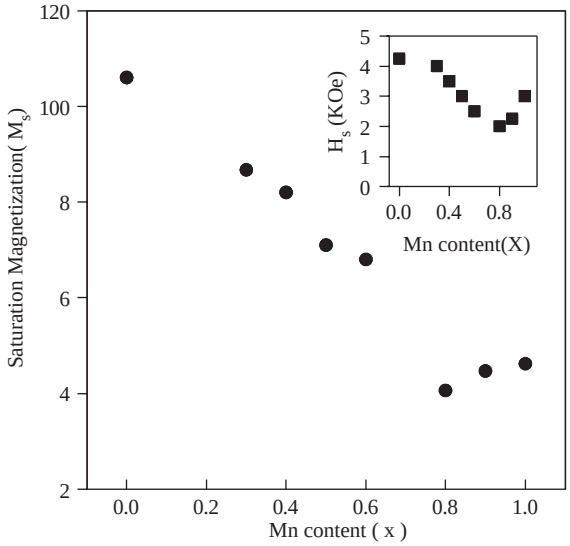

Figure 9. The saturation magnetization as a function of Mn content.

Assuming anti-parallel interaction, the theoretical magnetic moment is given by

$$\mu_{th} = (5.8 - x)\mu_B, \tag{5}$$

where x is the value of Mn content. The experimental value of magnetic moments μ_{ex} were obtained by the formula [17]

$$\mu_{ex} = \frac{MW \cdot M_s}{5585 d_s}. \tag{6}$$

The experimental magnetic moment decreases by increasing Mn content, as shown in Figure 10. The magnetic moment estimated from x-ray analysis was given by considering $1\mathrm{Mn}^{2+}$, $0.6\mathrm{Fe}^{3+}$ and $0.4\mathrm{Zn}^{2+}$ ions at A sites and $0.6\mathrm{Co}^{2+}$, $(x-t)\mathrm{Mn}^{3+}$ and $1.4{-}x+t$ ions at B sites, and has values near μ_{th}. The deviation between theoretical magnetic moment and experimental magnetic moment may be due to the fact that the structure does not have a completely inverse character. The magnetic moment of the divalent ions $= gM_s\mu_B$,

where g has the value 2. In the studied samples g may differ from this value. The deviation may also due to triangular moment of spin, which was treated theoretically by Yafet and Kittel angle [18]. The increase in magnetic moment M_s above $x = 0.8$ indicate the canting and the non-co linearity of the spin. This leads to the presence of spin vectors at B-sites, which makes a specific angle, and is responsible for the reduction of the $B-B$ exchange interactions, which increases the net magnetic moment of the samples. The canting and the change in the magnetic moment ordering with Mn addition are observed by measuring $Y-K$ angle. The values of $Y-K$ angle have been calculated using the formula $\mu_{exp} = (6+x)\cos\alpha_{y-k} - 5(1-x)$ where μ_{exp} is expressed in the units of Bohr magneton. These values are listed in Table 4. The $Y-K$ angle increases and reaches 73.6° at $x = 1$ and equal to zero for the samples with $x = 0.0$, 0.3 and 0.4.

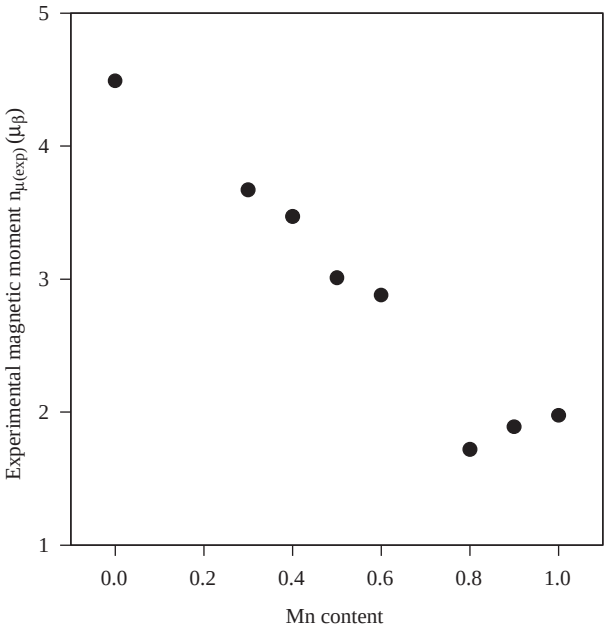

Figure 10. Experimental magnetic moments as a function of Mn content.

The behavior of magnetic moment with Mn addition can be divided into two regions. In the first one the Neel's theory is applied [19], in which there is a strong negative interaction between ionic moments at$A$ and B sites. The second region above $x = 0.8$, where the increase of the magnetic moment and the reduction of $B-B$ interaction with the substitution of Mn is demonstrated by the presence of non-collinear arrangement on the B-sites. The non-colinearity in B sites is reflected by the presence of $Y-K$ angle between the magnetic moment, which is responsible for the deviation from Neel's model and hence increases the magnetization. The difference between μ_{th} and μ_{ex} increases at higher values of Mn content due to the increase of $Y-K$ angle and the occurrence of non-colinearity of magnetic moment at B-site. The increase of magnetization is due to the increase of spin contribution by increasing the particle size. The effect of pores on magnetization appears in the first region where the magnetization decreases. The pores created demagnetizing field, and causes a rotation of magnetization away from the easy direction or nucleation of reverse domains.

The magnetic data is given in Table 4.

Table 4. The saturation magnetization, the magnetic moment and the Yafet-Kittel angle.

X	σ_s (emu/g)	μ_{ex} (μ_B)	μ_{x-ray} (μ_B)	μ_{th} (μ_B)	α_{Y-K}
0	106	4.49	5.8	5.8	0
0.3	86.7	3.67	5.42	5.5	0
0.4	82	3.47	5.29	5.4	0
0.5	71	3.01	5.17	5.3	32.04
0.6	68	2.88	5.05	5.2	42.32
0.8	40.6	1.72	4.81	5	66.42
0.9	44.7	1.89	4.66	4.9	69.73
1	46.2	1.97	4.54	4.8	73.61

4. Conclusion

By varying the Mn content the magnetic moment of all samples changed. The magnetic moment was theoretically calculated using the cation distribution from XRD and compared with the value calculated using experimental saturation magnetization observed from magnetizing curves. The differences in μ_{th} and μ_{ex} can explaining by considering the magnetic interaction, non-linearity and the canting effect; which are responsible for this differences. M_s decreases with increasing Mn content due to the decrease of A-B negative interaction. At $x = 0.8$, there is canting effect for the magnetic moment at Bsites, which decreases the negative $B - B$ anti-ferromagnetic interaction and increases the magnetization of$B$ sites; hence the net magnetization increase. The effect of $B - B$ interaction is usually masked by the strong $A - B$ interaction. The cation distribution was calculated from x-ray data analysis and the Mn addition substitute Fe^{3+} at tetrahedral and octahedral sites. The theoretical and experimental lattice parameters were nearly similar. The radius of tetrahedral sites, the bond length at tetra and octahedral sites increases by increasing Mn content, so the covalent character of the given ferrite decreased. The calculation of oxygen positional parameter indicates some deviation from the ideal value of 0.375 for the FCC lattice by increasing Mn content. The average grain size was calculated for all samples and was found within the spinel limits. The particle size was increase by increasing Mn content. The results show that there is a correlation between particle size and porosity with the structural and magnetic properties of the given samples.

Acknowledgment

The author briefly introduce his deep thanks to Professor Dr, Nabil Lahaam , the director of The Center of Theoretical and Applied physics Science (Ctaps) ,Yarmook University, Jordan, for offering the scientific visit to do this research.

References

[1] T. Nakamura and Y. Okano, *J. Appl. Phys.* **79, 1**, (1996), 475.

[2] T. Sato and Y. Sakaki, *IEEE Trans. Magn*, **26**, (1990), 2894.

[3] T. Akashi, *Trans-Jpn. Inst. Metals,* **2,** (1961), 171.

[4] K. Latha and D.Ravinder, *Phys. Stat. Sol (a)* **139**, (1993), 109.

[5] P.J. Van der Zaag, M. Kolenbrander and M. Th. Rekveldt. *Journal of applied Physics*, **83, 11**, (1998), 6870.

[6] K. Takadate, Y. Yamamoto, A. Makino, T. Yamaguchi and I. Sasada, *Journal of Applied Physics*, **83**, **11**, (1998), 6854.

[7] F.K. Lotgering, *J. Phys. Chem. Solid*, **25, 95**, (1964), 345.

[8] N.V. Belov Yamzin and Y. Z. Nozik, *J. Phys. Soc. Japan*, 17, suppl. B. 111, **55**, (1962), 261.

[9] N. Reslescu and E. Cuciureanu, *Phys. Status solidi (A).* **3**, (1970), 873.

[10] E.W. Gorter, C.O. Arean, *J. Chem. Soc. Dalton Trans*, (1985), 2155.

[11] International Tables of X-ray crystallography, vol. 1, Kynock press, Birmingham, p 320.

[12] K.J. Standly, *(Oxides Magnetic Materials*) Clarendon press, Oxford (1972).

[13] B.F. Levine, *Phys. Rev.* **B7**, (1973), 2591.

[14] K. Radha and D. Ravinder., Ind. *J. Pure Appl. Phys.* **33**, (1995),74.

[15] S.R. Sawant, S.S. suryavanshi, *Curr. Sci.* **57**, (12) (1988), 1276.

[16] G.K. Joshi, A.Y. Khot and C. R. Swaqnt, *Solid State Comm.***65, 12**, (1988), 1593.

[17] Mazharuddin Rana, Ph.D thesis Bahauddin Zakarya University, Pakistan (1998).

[18] Y. Yafet and C. Kittel, *Phy. Rev.* **87 (2)**, (1952), 290.

[19] I. Neel., *Annls. Phys.*, **3**, (1948), 137.